

Probabilistic Characterization of Sweep and Ejection Events in Turbulent Flows: Insights from Direct Numerical Simulation Data

Kuang-Ting Wu¹, Christina W Tsai¹, and Men-Jie Wu¹

¹National Taiwan University

November 24, 2022

Abstract

Turbulent boundary layers are populated by a hierarchy of recurrent structures normally referred to as “coherent structures.” Among others, ejection and sweep events are critical coherent structures of large-scale motions in turbulent flows. This study focused on gaining a better understanding of the spatial-temporal probabilistic characteristics of sweep and ejection events. The existence of uniform momentum zones (UMZs) is demonstrated to affect the spatial distribution of large-scale motions, and the ejection and sweep events tend to present near UMZ edges. On the basis of such observations, we considered the effect of UMZ edges on the presence of ejection and sweep events. In the current study, UMZ detection was employed to identify coherent structures. Several criteria for identifying coherent structures are revisited, and an integrated standard is applied to the available direct numerical simulation (DNS) turbulent channel flow data after UMZ edges were determined. Based on the integrated criterion for distinguishing ejection and sweep events, one can determine the probabilistic characteristics of coherent structures such as the maximum height, wall-normal length and streamwise length. Physical insights from DNS data such as joint probability density functions of wall-normal length and streamwise length can be established. The attached and detached features of the sweep and ejection coherent structures can then be classified and characterized, respectively. Durations of sweep and ejections events were demonstrated to follow a lognormal distribution in this study. The occurrence ratio of sweep events in the large-scale motions (LSMs) was quantified from the DNS data.

33 Abstract

34 Turbulent boundary layers are populated by a hierarchy of recurrent structures normally
35 referred to as “coherent structures.” Among others, ejection and sweep events are critical coherent
36 structures of large-scale motions in turbulent flows. This study focused on gaining a better
37 understanding of the spatial-temporal probabilistic characteristics of sweep and ejection events.
38 The existence of uniform momentum zones (UMZs) is demonstrated to affect the spatial
39 distribution of large-scale motions, and the ejection and sweep events tend to present near UMZ
40 edges. On the basis of such observations, we considered the effect of UMZ edges on the presence
41 of ejection and sweep events. In the current study, UMZ detection was employed to identify
42 coherent structures. Several criteria for identifying coherent structures are revisited, and an
43 integrated standard is applied to the available direct numerical simulation (DNS) turbulent channel
44 flow data after UMZ edges were determined. Based on the integrated criterion for distinguishing
45 ejection and sweep events, one can determine the probabilistic characteristics of coherent
46 structures such as the maximum height, wall-normal length and streamwise length. Physical
47 insights from DNS data such as joint probability density functions of wall-normal length and
48 streamwise length can be established. The attached and detached features of the sweep and ejection
49 coherent structures can then be classified and characterized, respectively. Durations of sweep and
50 ejections events were demonstrated to follow a lognormal distribution in this study. The
51 occurrence ratio of sweep events in the large-scale motions (LSMs) was quantified from the DNS
52 data.

53 **Keywords:** turbulent flows; coherent structures; conditional velocity decomposition; probability
54 distributions; large scale motions; DNS data

55 1. Introduction

56 Sediment transport in open channel flow has a significant impact on the siltation of rivers,
57 reservoirs, and artificial channels, and it is one of the major topics studied in the water resources
58 realm. Despite the intensive investigation done in the past, the transport mechanism of sediment
59 particles seems to have reached a stage where further progress may depend on a more
60 comprehensive understanding of the chaotic and intermittent behavior of turbulence. Among
61 others, the existence of coherent structures in wall-bounded turbulent flows has been confirmed.
62 Such turbulent structures play a dominating role not only in the movement of sediment particles
63 but also in determining mean flow, stress and other statistical properties. For example, the coherent
64 structures near the bed tend to have a large momentum exchange, leading to increased Reynold
65 shear stress near the bed (MacVicar & Roy, 2007; Truong & Uijttewaal 2019; and Wang et al.
66 2021). Zhong et al. (2016) discovered that strong super-streamwise vortices might cause erosion
67 and sedimentation in the downwelling and upwelling sides, respectively.

68 It has been shown that transport of sediment particles is closely related to some coherent
69 structures defined as the ejection (Q2) and sweep (Q4) events (Chang et al., 2011; Dwivedi et al.,
70 2011; Muste and Yu, 2005). Hurther and Lemmin (2003) indicated that ejection (Q2) and sweep
71 (Q4) events tend to entrain the particles into suspension and to move particles near the bed,
72 respectively. Lelouvetel et al. (2009) proposed that over 70% of coherent structures observed at
73 particle incipient motion in turbulent flows can be classified as ejections (Q2) and sweeps (Q4).
74 The influence of ejection and sweep events on sediment entrainment is reported (Nino and Garcia,
75 1996; Dwivedi et al., 2011). These two coherent structures also influence the instantaneous local

76 sediment concentration in the near-wall region (Cellino and Lemmin, 2004; Noguchi and Nezu,
77 2009; Salim et al., 2017).

78 Moreover, these coherent structures disturb sediment particles for a particular period and
79 carry particles over long distances, resulting in the temporal and spatial correlations of flow
80 velocities in the flow field (Cellino & Lemmin 2004; Okamoto, Nezu & Katayama 2010). Chen,
81 Sun & Zhang (2013) presented a model that is based on the fractional advection-diffusion equation
82 to account for the long distances over which sediment particles are carried by large turbulent
83 structures. More recently, Tsai and Huang (2019) and Tsai et al. (2021) have shown that when
84 particles transport within time-persistent turbulent flow structures, the movements of the sediment
85 particles may exhibit persistency that depends on the various temporal durations of turbulent flow
86 structures.

87 Based on the observations mentioned above, the coherent structures are found to be critical
88 in affecting the probabilistic behavior of sediment particles. It is desirable to better understand and
89 quantify the spatial and temporal characteristics of turbulent flows, particularly the sweep and
90 ejection events so that the influence of turbulent coherent structures on sediment particle
91 movement can be more precisely evaluated. This study aims at answering the following
92 fundamental questions. (1) What is the probability distribution of the maximum height of the event
93 occurrences? (2) How to describe the geometrical structure (spatial scales) of the sweep and
94 ejection events in a probabilistic manner? And (3) How to statistically characterize the duration
95 (temporal scales) of the sweep and ejection events?

96 **2. Turbulent Coherent Structure and Uniform Momentum Zones (UMZs)**

97 In turbulence research, it is acknowledged that deconstructing complex turbulence into
98 more characteristic elementary components would provide additional information about its nature.
99 On the basis of their laboratory experiments, Grass (1971) and Wallace et al. (1972) indicated that
100 turbulence is generated by intermittent coherent structures (burst cycles) near the boundary. Since
101 then, many studies have presented evidence that the turbulent boundary layer (TBL) is populated
102 by a hierarchy of coherent structures such as low- and high-speed streaks (Offen & Kline, 1975),
103 ejections and sweeps (Wallace et al., 1972), streamwise vortices (Blackwelder & Eckelmann,
104 1979), hairpin vortices (Offen & Kline, 1975) large-scale bulges (Falco, 1977), hairpin vortex
105 packets (Adrian et al., 2000), very large-scale motions (VLSMs) (Kim & Adrian, 1999), and
106 superstructures (Hutchins & Marusic, 2007). In their extensive study on the TBL structure, Smits
107 et al. (2011) summarized the scaling laws, generation and interaction mechanisms, and their roles
108 in the production and dissipation of these coherent structures. Moreover, Adrian and Marusic
109 (2012) analyzed hairpin and packet-like structures to determine these structural properties.

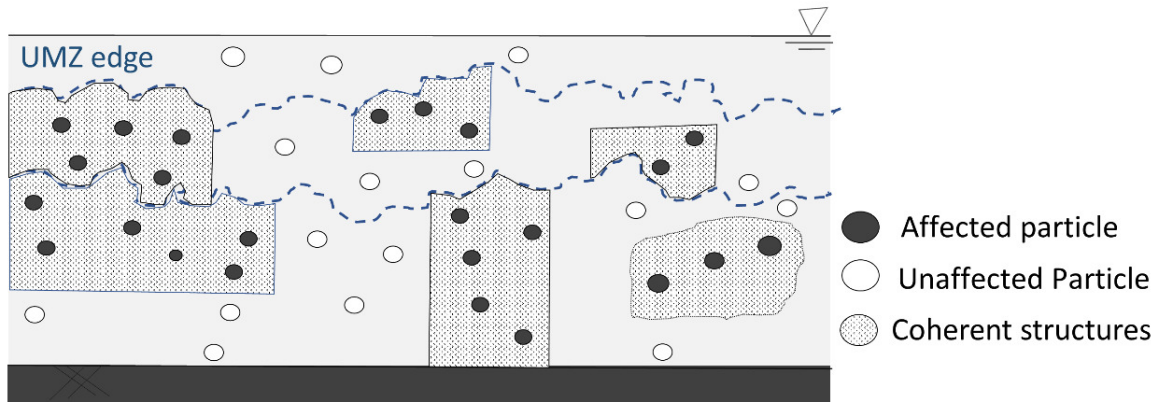
110 Regarding the characteristic spatial scales (e.g., geometry) of turbulent structures, Meinhart
111 and Adrian (1995) first highlighted the existence of large and irregularly shaped regions of uniform
112 streamwise momentum zones (hereafter, UMZs), regions of relatively similar streamwise velocity
113 with coherence in the streamwise and wall-normal directions. It is observed that these UMZs
114 generally encapsulated the near-wall region. Accordingly, the boundary layer is divided into
115 several zonal structural arrangements and demarcated by thin interfacial layers of strong shear,
116 where most of the vorticity is clustered in the TBL (Adrian et al., 2000; Eisma et al., 2015). The
117 relationship of large-scale motions (LSMs) such as ejection and sweep events with the existence
118 of UMZs is debated. Based on these works, de Silva et al. (2016) provided insight into how

119 instantaneous phenomena such as a zonal-like structural arrangement can be separated by UMZ
120 edges.

121 de Silva et al. (2017) also provided a detection criterion that had previously been used to
122 locate UMZs and demonstrated the application of this criterion to estimate the spatial locations of
123 the edges that demarcate UMZs. They also demonstrated the regulation of the presence of ejection
124 (Q2) and sweep (Q4) events, which occur below and above the interface, respectively. Hence, the
125 LSMs' spatial distribution is confirmed to be affected by the existence of UMZs.

126 Owing to advances in particle image velocimetry (PIV) and direct numerical simulation
127 (DNS), which researchers of turbulence structures in TBLs can draw from, the presence of a
128 pronounced zonal-like structure in instantaneous fields of streamwise velocity fluctuations has
129 been revealed. That is, the TBL includes several regions of roughly uniform streamwise velocity
130 magnitudes, called the UMZ. Meinhart and Adrian (1995) observed that a UMZ edge separates
131 the neighboring UMZs with a strong shear originating from concentrated patches of vortices. de
132 Silva et al. (2016) also demonstrated that sudden step-like jumps exist in the streamwise flow
133 velocity profile. Therefore, streamwise velocities within UMZs are bounded by distinct step
134 changes in streamwise momentum, which indicate that shear layers of intense vorticity separate
135 each zone. Specifically, these UMZs are demarcated by thin interfaces of strong shear that indicate
136 a large proportion of the vorticity is clustered in the turbulent boundary layer (TBL).

137 The organized vortical structures that contort UMZ interfaces are a manifestation of
138 ejection events and sweep events around the interface (Ganapathisubramani et al., 2003; Saxton-
139 Fox & McKeon, 2017; Tomkins & Adrian, 2002), demonstrating that UMZ edges and the spatial
140 distribution of LSMs affect each other. In this study, discrimination of the interfaces of UMZs is
141 an essential step in estimating the spatial-temporal characteristics of LSMs. **Figure 1** illustrates
142 the potentially impacted region in TBL on sediment particles due to turbulent coherent structures.



143
144 **Figure 1.** Conceptual vertical section with an ejection event
145

146 3. Description of DNS data

147 Lee and Moser (2014) used DNS to obtain channel flow data, which are available online
148 in the Johns Hopkins Turbulence Databases (JHTDB; <http://turbulence.pha.jhu.edu>). The
149 simulation we analyze here is DNS of incompressible turbulent flow between two parallel planes,
150 and no-slip condition/no-penetration boundary condition is applied on the wall. Details of the
151 experimental parameters of JHTDB are summarized in **Table 1**. It should be mentioned that the
152 time step we utilized is 0.05 sec, which is smaller than the time scale of experimental physical

153 phenomena, i.e., the duration of coherent structures. Based on LeHew et al. (2013) regarding the
 154 lifespan of coherent structures, the shortest duration they observed is about 0.1 sec. The time step
 155 (0.05 sec) in this study is suitable for capturing the temporal distribution of coherent structures.

156
 157 **Table 1.** Experimental parameters of JHTDB employed. L_x and L_y correspond to the field of
 158 view of the streamwise wall-normal plane, and h is the half channel height. It should be noted
 159 that because $U_c \neq U_\infty$ in JHTDB, we assume the maximum of measured velocity equal to U_∞ .

Friction velocity Reynolds number Re_τ	Viscosity ν	Domain Length $L_x \times L_y$	Centerline velocity $U_c (ms^{-1})$	Friction velocity $u^* (ms^{-1})$	half channel height $\delta (m)$
5186	8×10^{-6}	$8\pi \times 2$	1.1	0.041	1.0

160 This database was selected because it includes data on wall-bounded turbulent flows with
 161 high Reynolds numbers. Moreover, the DNS feature of this database can provide detailed
 162 information about the generating role of LSMs that would not otherwise be available. Therefore,
 163 the current study aimed at gaining further physical insight into the probabilistic spatial and
 164 temporal scales and other characteristics of sweep and ejection coherent structures in turbulent
 165 flows.

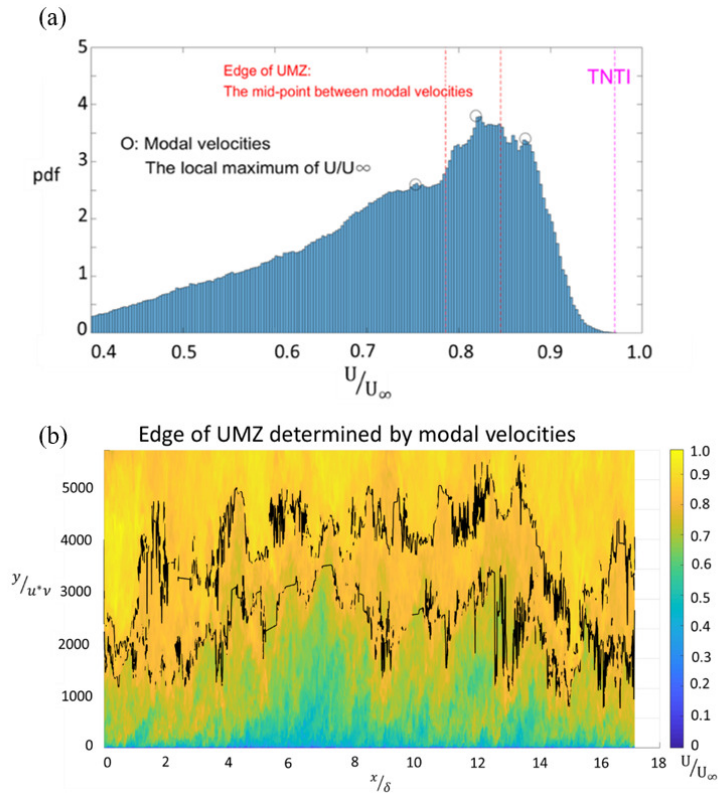
166

167 4. Detection of UMZs

168 Instantaneous UMZs were detected using the methodology of Adrian et al. (2000) and de
 169 Silva et al. (2016, 2017). According to these studies, UMZs were detected from the local maxima
 170 in the probability density functions (PDFs) of the streamwise velocity components. These distinct
 171 local maxima, which are related to the streamwise momentum of each UMZ in the PDFs, represent
 172 large regions of the flow that develop downstream at relatively constant velocity magnitudes or
 173 modal velocities. The magnitude of the streamwise velocity that demarcates each detected UMZ
 174 is approximated by the midpoint between modal velocities of neighboring UMZs. **Figure 2**
 175 displays the detection criterion employed in this study. **Figure 2(b)** presents an instantaneous
 176 velocity field obtained from JHTDB whose $Re_\tau \approx 5,200$. The corresponding PDF of the
 177 streamwise velocity is presented in **Figure 2(a)**, where the peaks of this PDF are referred to as
 178 modal velocities (indicated by \circ symbols). Notably, $y^+ = 0$ represents the location in the upmost
 179 boundary layer, whereas $y^+ = 5,500$ indicates the location on the boundary.

180 In this study, the spatial location of the UMZ was determined using a streamwise velocity
 181 magnitude (**Figure 2**). Notably, de Silva et al. (2016) estimated the location of the turbulent–non-
 182 turbulent interface (TNTI) by using a constant streamwise velocity magnitude of $97\%U_\infty$ to
 183 minimize the influence of applying the various detection criteria used for the TNTI and the UMZ
 184 edges. However, because the streamwise velocity magnitude of $97\%U_\infty$ is insufficient for clearly
 185 drawing the TNTI, the TNTI is not included in our discussion. **Figure 2(a)** displays three clear
 186 peaks in the PDFs (modal velocities), whose corresponding UMZs are also detectable (**Figure**
 187 **2(b)**). The detected UMZ edges are represented by the solid lines, which are overlaid on iso-
 188 contours of streamwise velocity. Therefore, after the detection of UMZ edges, two UMZ edges
 189 appear in this flow field. As indicated, the location of the upper UMZ edge appears at $y^+ \approx 3,900$,

190 and the location of the lower UMZ edge appears at $y^+ \approx 1,600$. Srinath (2017) proposed a
 191 threshold which is y^+ is larger than $0.1\delta^+ \approx 500$; then the region called the outer region. Thus,
 192 compared with the general stratification of TBL, the UMZ edges exist in the outer region of TBL.



193 **Figure 2.** Illustration of the detection of instantaneous UMZs. (a) The corresponding histogram
 194 of U/U_∞ ; vertical dashed lines represent the streamwise velocity of the detected UMZ edges. (b)
 195 UMZ edges determined using modal velocities overlaid on iso-contours of streamwise velocity
 196 (U). the color bar for the study area ($0 \leq x/\delta \leq 17, 0 \leq y^+ \leq 5,500$) is on the right.
 197
 198

199 5. Instantaneous Flow Velocity Decomposition

200 Before directly extracting the characteristics of coherent structures from the database, we
 201 conducted velocity decomposition to quantify the mean velocity and corresponding velocity
 202 fluctuation. Based on the magnitude of the mean fluid velocity and its fluctuations, coherent
 203 structures can be extracted from the DNS data. Reynolds decomposition is widely used for
 204 analyzing velocity fields. Accordingly, Reynolds decomposition, whose general form is presented
 205 in Equation 1, is typically employed to evaluate the fluctuating component of velocity in the
 206 analysis of velocity fields in a certain region of the TBL.

$$207 \quad u = \bar{u} + u' \tag{1}$$

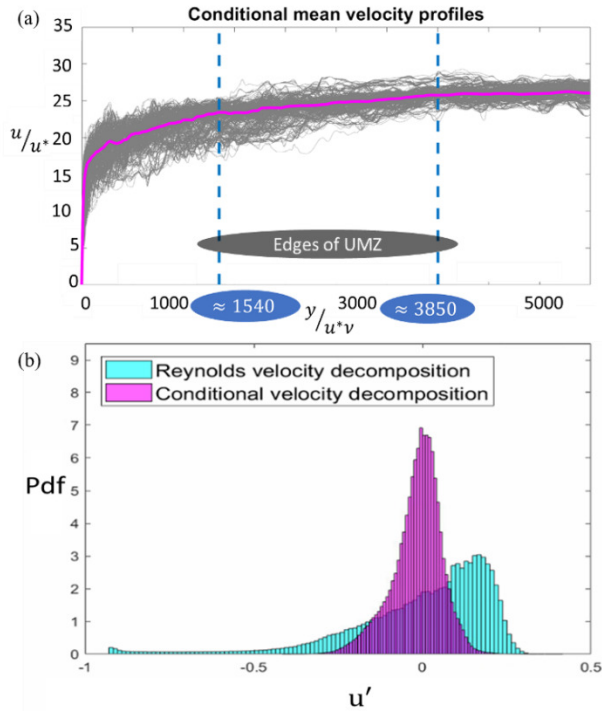
208 where u is total flow velocity, \bar{u} is mean flow velocity, and u' is the velocity fluctuation. The
 209 distribution of u' is dependent on the properties of the flow field.

210 The statistical properties of flow velocities involve fluid particle movement information.
 211 In the current study, such information was used to represent the flow structures in the wall-bounded

212 flow. However, the analyses were extended into the whole TBL region, where streamwise velocity
 213 becomes lower nearer to the wall; therefore, the near-wall sweep event might be eliminated
 214 because of the use of a conventional mean. That is, under the Reynolds decomposition, both
 215 ejection and sweep events might be reduced to background fluctuation under the threshold of the
 216 traditional mean.

217 The characterization of each flow region is independent of all other regions, which cannot
 218 be isolated under the Reynolds decomposition. Thus, in the current study, the conditional mean
 219 might be an appropriate method for decomposing the total velocity. The separation of turbulent
 220 and non-turbulent regions using different mean velocities was first attempted by Antonia (1972)
 221 and Hedley and Keffer (1974). Subsequently, Antonia et al. (1975), Fabris (1979), and Gutmark
 222 and Wygnanski (1976) observed various zonal mean velocities in different respective regions and
 223 defined the fluctuation of velocity regarding the zonal mean velocities for each respective region
 224 instead of using Reynolds-averaged mean velocities.

225 Recently, Kwon et al. (2016) and Lee et al. (2017) proposed a new decomposition approach
 226 in which the mean velocity is a function of not only the wall-normal distance but also the height
 227 of the TNTI interface (i.e., it is the outermost UMZ edge in the TBL). In our application, we
 228 followed their procedure and treated the mean velocity as a function of both the wall-normal
 229 distance and the height of UMZ edges. Our results are presented in **Figure 3(a)**, where the red line
 230 represents the ensemble mean of the conditional mean velocity profiles, which satisfy the values
 231 of the UMZ edges represented by the blue dotted lines.



232 **Figure 3.** (a) Conditional mean velocity profiles. (b) Histograms of streamwise velocity
 233 fluctuation.
 234

235 **Figure 3(b)** displays the comparison of the PDF of streamwise velocity fluctuations based
 236 on the Reynolds and conditional decomposition. Here, the blue PDF represents the distribution
 237 obtained from Reynolds velocity decomposition, whose range of fluctuations is wider than that of

238 conditional velocity fluctuations (the red PDF), which were obtained by considering the spatial
 239 variation of the mean velocity. Therefore, considering the spatial distribution of structures yields
 240 a conditional velocity decomposition that is more suitable for capturing the coherent structures
 241 than is Reynolds decomposition, in which the mean velocity is a single value. After obtaining the
 242 conditional mean velocity profile, we further applied the identified criterion, which was used to
 243 capture the physical properties of the coherent structures.

244 6. Identification of Coherent Structures

245 Identifying the coherent structures in a TBL depends on knowing the mechanics of
 246 turbulence, which is provided by understanding the characteristics of a group of eddies that
 247 sufficiently manifest the flow dynamics. Accordingly, this section examines the dynamics of the
 248 TBL in terms of the temporal evolution of coherent structures. Coherent structures are organized
 249 in space and persistent in time. However, the literature provides various criteria for identifying
 250 coherent structures. Several well-known methods are revisited, and an integrated standard is
 251 applied.

252 6.1 Criteria for Identifying Coherent Structures: Q Criterion

253 Although no consensus has been reached on the mathematical definition, coherent
 254 structures are intuitively accepted by the fluid dynamics community as three-dimensional (3D)
 255 tube-shaped structures with spatially limited distributions of concentrated vorticity (Jeong et al.,
 256 1997; Kaftori et al., 1994; Robinson, 1991). The vorticity magnitude was first used to identify the
 257 vortex tube (She et al., 1990). However, because the vorticity method was insufficient for
 258 distinguishing between vortex cores and shear motions, the method was later replaced by more
 259 robust criteria based on the local velocity gradient tensor, which was used to identify the vortex
 260 tube in 3D velocity fields (Hunt et al., 1988; Jeong & Hussain, 1995; Nagaosa, 1999).

261 Hunt et al. (1988) developed the Q criterion for a full velocity gradient tensor in
 262 incompressible flows; the second invariant Q can be written as

$$263 \quad Q = \frac{1}{2} (\|\Omega\|^2 - \|S\|^2) \quad (2)$$

264 where Ω is the rate-of-rotation tensor corresponding to pure rotational motion and S is the rate-of-
 265 strain tensor corresponding to pure irrotational motion.

$$266 \quad \Omega = \frac{1}{2} [\nabla U - (\nabla U)^T] \quad (3)$$

$$267 \quad S = \frac{1}{2} [\nabla U + (\nabla U)^T] \quad (4)$$

268 Hence, the second invariant is a local measure of the excess rotation rate relative to the strain rate.
 269 For a two-dimensional (2D) velocity gradient tensor, Equation 1 can be simplified to

$$270 \quad Q = -\frac{\partial u}{\partial y} \frac{\partial v}{\partial x} - \frac{1}{2} \left(\frac{\partial u}{\partial x} \right)^2 - \frac{1}{2} \left(\frac{\partial v}{\partial y} \right)^2 \quad (5)$$

271 where connected regions of positive Q are defined as vortices, and $Q > 0$.

272 6.2 Criteria for Identifying Coherent Structures: λ_{ci} criterion

273 The use of vorticity and kinematics implied by the velocity gradient tensor has been
 274 reported. Zhou et al. (1999) proposed the use of the imaginary part of the complex eigenvalue of

275 the local velocity gradient tensor as an unambiguous measure of rotation and the commonly named
 276 swirling strength. Unlike vorticity, swirling strength, λ_{ci} , (i is not an index in this definition but
 277 an abbreviation for the word "imaginary") does not highlight regions of intense shear. The swirling
 278 strength criterion has been demonstrated to be an adequate identifier of vortex cores (Adrian et al.,
 279 2000).

280 Similar to the 3D form, the 2D form of the λ_{ci} criterion is based directly on the Δ criterion.
 281 On the basis of the 2D velocity gradient tensor, the λ_{ci} indicator can be computed as

$$282 \quad \lambda_{ci} = \frac{1}{2} \sqrt{-4 \frac{\partial u}{\partial y} \frac{\partial v}{\partial x} - \left(\frac{\partial u}{\partial x} - \frac{\partial v}{\partial y} \right)^2} \quad (6)$$

283 6.3 Criteria for Identifying Coherent Structures: λ_2 criterion

284 Nagaosa (1999) revealed that a layer-like coherent structure is frequently misidentified as
 285 a vortex tube, particularly in the near-wall region, when vorticity is used as an indicator. To avoid
 286 such mistakes, the researchers applied the indicator developed by Jeong and Hussain (1995). The
 287 aforementioned indicator is based on the observation that a local pressure minimum corresponds
 288 well with the vortex center, except in the presence of strong, unsteady, and viscous effects.
 289 Moreover, on the basis of the 2D velocity gradient tensor, λ_2 can be computed as

$$290 \quad \lambda_2 = \frac{\partial u}{\partial y} \frac{\partial v}{\partial x} + \frac{1}{2} \left[\left(\frac{\partial u}{\partial x} \right)^2 + \left(\frac{\partial v}{\partial y} \right)^2 + \left| \frac{\partial u}{\partial x} + \frac{\partial v}{\partial y} \right| \sqrt{\left(\frac{\partial u}{\partial x} - \frac{\partial v}{\partial y} \right)^2 + \left(\frac{\partial u}{\partial x} + \frac{\partial v}{\partial y} \right)^2} \right] \quad (7)$$

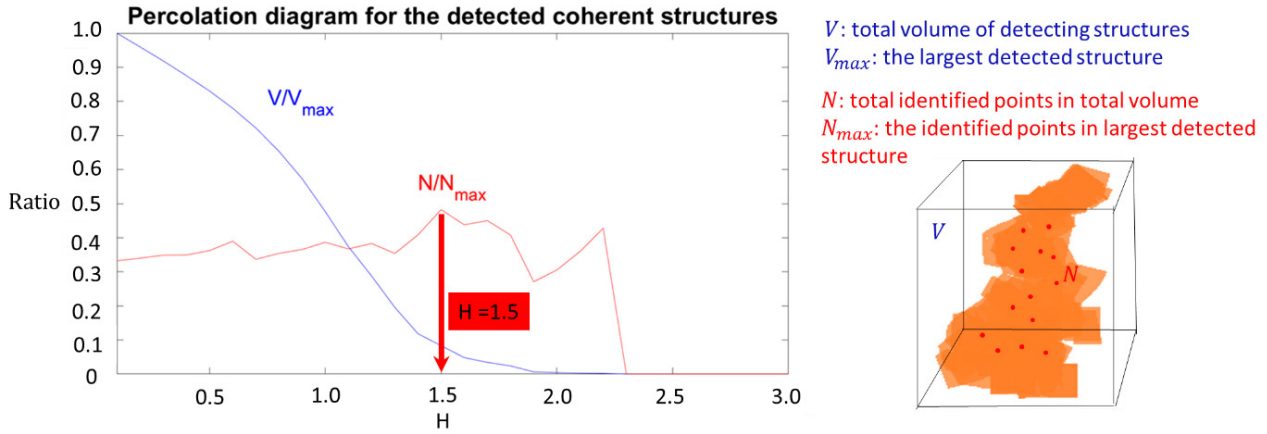
291 where the region satisfying $\lambda_2 < 0$ can be identified as vortices.

292 Coherent structures such as well-organized quasi-streamwise vortex tubes or bursting
 293 events are intermittently generated by near-wall turbulence. Therefore, a spatial illustration after
 294 the Q criterion, λ_{ci} criterion, or λ_2 criterion is applied as an overview of vortices. If structures such
 295 as sweep and ejection events must be distinguished, then relevant criteria should be integrated to
 296 provide a more rigorous definition of coherent structures.

297 6.4 Criteria for Identifying Coherent Structures: H Criterion

298 Ferreira et al. (2002) and Lu and Willmarth (1973) defined a threshold that allows the
 299 commonly named hole-size H to be used for detecting ejection and sweep events. Yoon et al.
 300 (2020) then defined the coherent structures of u as groups of connected points where $u >$
 301 $H \times u_{rms}$ and $u < -H \times u_{rms}$ in instantaneous flow fields, where H is identified. However,
 302 different recommendations for the value of H have been proposed, affecting the result of structure
 303 detection. For example, H = 1.2, 1.5, 1.7, 1.75, 2.5, and 3 have all been proposed (Franca et al.,
 304 2014; Liu et al., 2016; Lozano-Durán et al., 2012; Nezu et al., 1994; Séchet & le Guennec, 1999;
 305 Yoon et al., 2020). In particular, Lozano-Durán et al. (2012) noted that the threshold depends on
 306 the wall distance. Therefore, the authors introduced the percolation theory to generate the statistics
 307 of connected components on a random graph. This theory can also be applied to extract the volume
 308 of connected eddies. del Álamo et al. (2006), Moisy and Jiménez (2004), and Yoon et al. (2020)
 309 first attempted to identify the vorticity and dissipation structures in isotropic turbulence, channels,
 310 and zero pressure gradient TBLs, respectively.

311 The percolation diagram of the identified coherent structures (**Figure 4**) was used to select
 312 H . The blue line is the ratio of the volume of the largest identified eddies, V_{max} , to the total volume
 313 V , satisfying the value of H from 0.1 to 3, whereas the red line indicates the total number of
 314 identified objects (N) normalized by its maximum (N_{max}), whose peak appears at $H \approx 1.5$. This
 315 behavior is consistent with the result of Yoon et al. (2020). The normalized volume (V/V_{max})
 316 increases as H decreases. As H decreases, new structures arise, or some of the previously detected
 317 objects gather. The balance between the two effects yields the peak in the variation of N/N_{max} .
 318 However, the value of H is a function of wall distance, as previously mentioned. Although the
 319 whole TBL is considered here, other studies have considered only a particular region in the TBL;
 320 therefore, our results do not reveal the peak clearly. In the present study, despite the unclear peak,
 321 $H \approx 1.5$ was selected on the basis of the percolation transition.



322
 323 **Figure 4.** Percolation diagram for the detected coherent structures. The variations within the total
 324 volume (V) and the total number (N) of objects are displayed.
 325

326 6.5 Criterion Comparison and Selection

327 Comparing Equations 5–7, Q , λ_{ci} , and λ_2 satisfy the following condition:

328
$$\frac{\partial u}{\partial y} \frac{\partial v}{\partial x} < 0 \tag{8}$$

329 To explore the similarities and differences among these equations, Chen et al. (2015)
 330 compared the aforementioned criteria using planar velocity fields extracted from both DNS and
 331 PIV datasets. Moreover, the researchers revealed that a mathematical relationship between these
 332 criteria could interpret the disparity among the identification of coherent structures. According to
 333 Equation 5–7, $Q > 0$ is a subgroup of $\lambda_{ci} > 0$, and $\lambda_2 < 0$ is a subgroup of $Q > 0$. Therefore, λ_2
 334 tends to eliminate the relatively weak vortices and make visible a snapshot of the structure
 335 identification, so we have used it herein. As mentioned, the structures discussed here are the
 336 commonly named Q_s events, which are detected using quadrant analysis. However, Ferreira et al.
 337 (2002) first revealed that quadrant analysis might lead to inadequate features. An individual
 338 turbulent event may be detected as a series of separate smaller events. Section 5.4 presented the
 339 modification of the quadrant threshold method. Comprehensively, the applied threshold criteria
 340 are as follows:

341 Ejection:

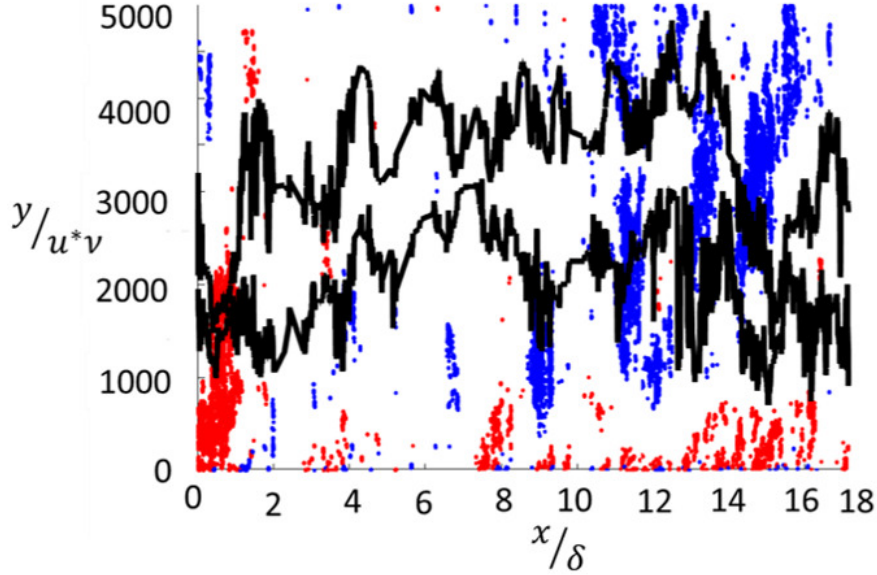
$$342 \quad Q_2 = \{(u < -1.5 \times u_{rms}) \wedge (u' < 0) \wedge (\lambda_2 < 0) \wedge (v' > 0)\}$$

343 Sweep:

$$344 \quad Q_4 = \{(u > 1.5 \times u_{rms}) \wedge (u' > 0) \wedge (\lambda_2 < 0) \wedge (v' < 0)\}$$

345 **Figure 5** illustrates the extracted coherent structures in the flow field based on the
346 integrated criterion.

347



348

349 **Figure 5.** Coherent structures are identified in a snapshot from the JHTDB. The blue points
350 represent the structures classified as sweep events, and the red points represent the structures
351 classified as ejection events. The black lines represent the UMZ edges.

352

353 6.6 Tracking the Duration of Sweep and Ejection Events

354 Time-resolved data were used to track the events over time, enabling the production and
355 dissipation of each event to be identified and the duration of each event to be determined. This
356 section describes the method used for tracking the sweep and ejection events over time. On the
357 basis of the assumption used by Fiscaletti and Ganapathisubramani (2018), if two events ev_1 and
358 ev_2 are detected consecutively, and the following condition holds, we treat them as the same event:

$$359 \quad d_{cent} < D_{box} \tag{9}$$

360 where d_{cent} is the distance between the centroids of ev_1 and ev_2 , and D_{box} is the diagonal of the
361 smallest rectangle, including all points of ev_1 , as depicted in **Figure 3(a)** (Yoon et al., 2020).

362 7. Characterization of LSMs in the TBL

363 Here, ejection and sweep events are referred to as LSMs. This section analyzes the results
364 of the JHTDB application of the detection criterion described in section 6.1 to determine the
365 spatial-temporal distribution of LSMs.

366 7.1 Spatial Distribution of Events

367 Regarding the spatial distribution of ejection and sweep events, Dennis and Nickels (2011)
368 conducted their analysis on the quasi-instantaneous 3D velocity fields of a TBL and observed that
369 strong vertical velocity fluctuations are adjacent to the large flow structures. Their results imply
370 that ejection and sweep events occur around structures with low and high streamwise velocities,
371 respectively. Tsai and Huang (2019) treated the histogram of the maximum heights reached by
372 structures with low and high streamwise velocities as representing the probabilities of ejection and
373 sweep events at various flow elevations. Dennis and Nickels (2011) suggested that the gamma
374 distribution can provide the best fit to the histogram of the maximum height.

375 In the current study, the structural properties, such as maximum height, streamwise and
376 wall-normal length, and duration, were extracted from the JHTDB. The flow condition under
377 which the JHTDB data were obtained differs from that of Dennis and Nickels (2011), causing the
378 structures to characterize somewhat differently.

379 **Figure 6** presents the probability density function of the maximum height of (a) ejection
380 and (b) sweep events. As presented in the figure, a low point at y^+ exists between 1,100 and 2,200,
381 where the upper UMZ edge is located. Moreover, the maximum height in the region between 1100
382 and 2200 in (a) and above 4,400 in (b) is similar to that described by de Silva et al. (2017), who
383 observed that sweep events are generally located above the UMZ edges, and ejection events are
384 generally located under the UMZ edges. In the current study, the two UMZ edges are located at
385 $y^+ \approx 1,540$ and $y^+ \approx 3,850$. After the sweep and ejection events occurred above the upper UMZ
386 edge and below the lower UMZ edge, respectively, they populated the entire UMZ region. This
387 phenomenon is consistent with Lozano-Durán and Jiménez (2014), who claimed that ejection
388 events appear in the near-wall region and rise, whereas sweep events appear away from the wall
389 and drop.

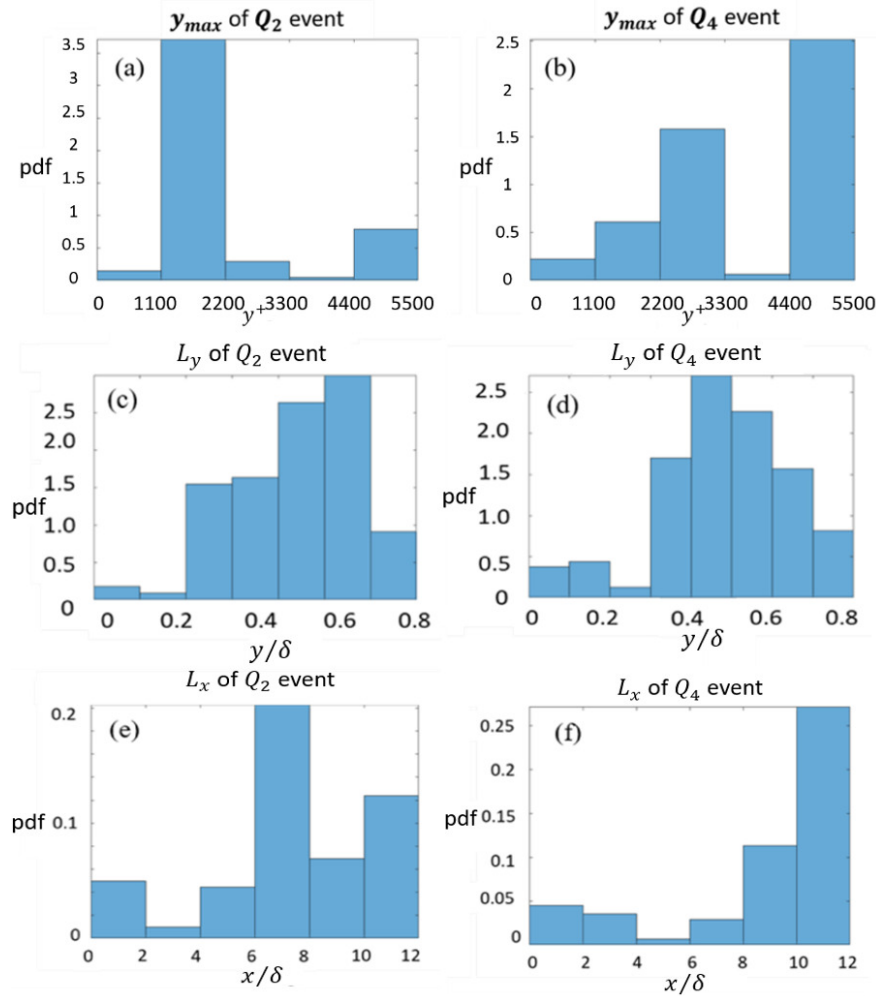
390 If an event occurs, its maximum height must be determined to be its upper boundary,
391 depending on the distribution presented in **Figure 6**(a & b). However, its lower limit is determined
392 in one of two manners, one of which was made evident by de Silva et al. (2017), who presented a
393 scenario in which the ejection and sweep events are likely to appear below and above the interface,
394 respectively. **Figure 6**(c & d) displays the distribution of the vertical lengths of LSMs. Because
395 the whole flow field is divided into three parts in the wall-normal direction after consideration of
396 the UMZ edges, the scale of wall-normal length (L_y) in this analysis is consistent with the results
397 of Yoon et al. (2020), who found that most L_y values range from 0.4δ to 0.6δ .

398 Tsai and Huang (2019) postulated that the flow region below the sampled maximum height
399 is affected by LSMs. This work established that the LSM length scales in the vertical direction are
400 also affected by the UMZ edges.

401 Regarding the streamwise LSM length, the properties of each event were extracted directly
402 from the dataset. The histogram of streamwise length represents the probability that the range in
403 the streamwise direction is influenced by ejection and sweep events (**Figure 6**(e & f)). Because of

404 the application of the criterion proposed by Fiscaletti and Ganapathisubramani (2018) into the
 405 spatial resolution of the identification of coherent structures, two consecutive events could be
 406 merging into a larger event. Although Dennis and Nickels (2011) used an exponential distribution
 407 to represent the streamwise LSM lengths, the distribution of both ejection and sweep events
 408 favored the more extended event.

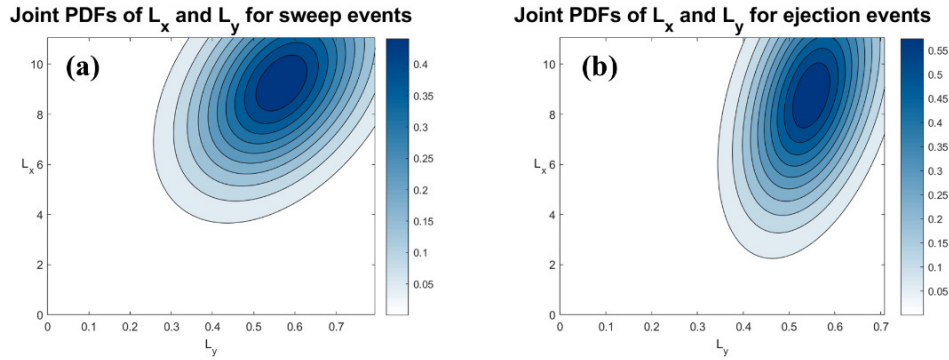
409



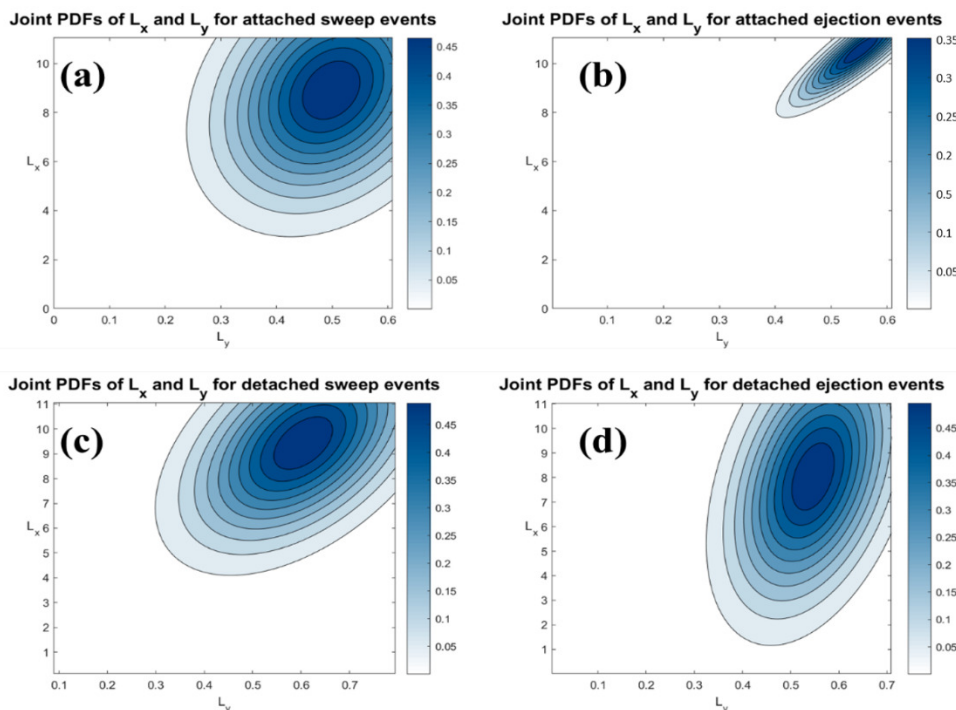
410
 411
 412
 413
 414
 415

Figure 6. Probability density functions of the maximum height of (a) ejection and (b) sweep events.; Probability density function of the wall-normal lengths of (c) ejection and (d) sweep events.; Probability density function of the streamwise lengths of (e) ejection and (f) sweep events.

416 The spatial features of the 2D LSMs were examined relative to the proposed formulas. The
 417 structures can be classified into attached and detached structures relative to the minimum y -
 418 position of structure y_{min} , where $y_{min} \approx 0$ refers to wall-attached structures, whereas $y_{min} > 0$
 419 refers to detached structures. That is, attached structures signify that the structure attaches to the
 420 wall, whereas detached structures suspend in the flow field. Herein, these identified structures were
 421 further classified into wall-attached and wall-detached structures, and the relationship between
 422 their characteristic lengths in streamwise and wall-normal directions is discussed.



423
424 **Figure 7.** Joint PDFs of L_x and L_y of (a) sweep and (b) ejection events.
425



426
427 **Figure 8.** Joint PDFs of L_x and L_y of (a) attached sweep, (b) attached ejection, (c) detached
428 sweep, and (d) detached ejection events.

429 **Figure 7** presents the joint PDFs of L_x and L_y of sweep and ejection events. The slope of
430 the joint PDF of ejection events is more tilted than that of sweep events, revealing that the vertical
431 variation of sweep events is more extensive than that of ejection events. However, ejection events
432 tend to exhibit more extended variation than do sweep events in the streamwise direction. That is,
433 as a sweep event occurs, its streamwise length will generally exceed that of an ejection event,
434 which is consistent with the findings of Dennis and Nickels (2011).

435 The results presented in **Figure 8**(a) and (c) indicate that despite the almost complete lack
436 of distinction between the distributions of attached or detached sweep events, the distribution of
437 detached sweep events is more similar to the distribution of entire sweep events. This phenomenon
438 indirectly confirms the finding that sweep events appear away from the wall and drop to dissipate.
439 Accordingly, sweep events are commonly named detached structures. By contrast, attached and

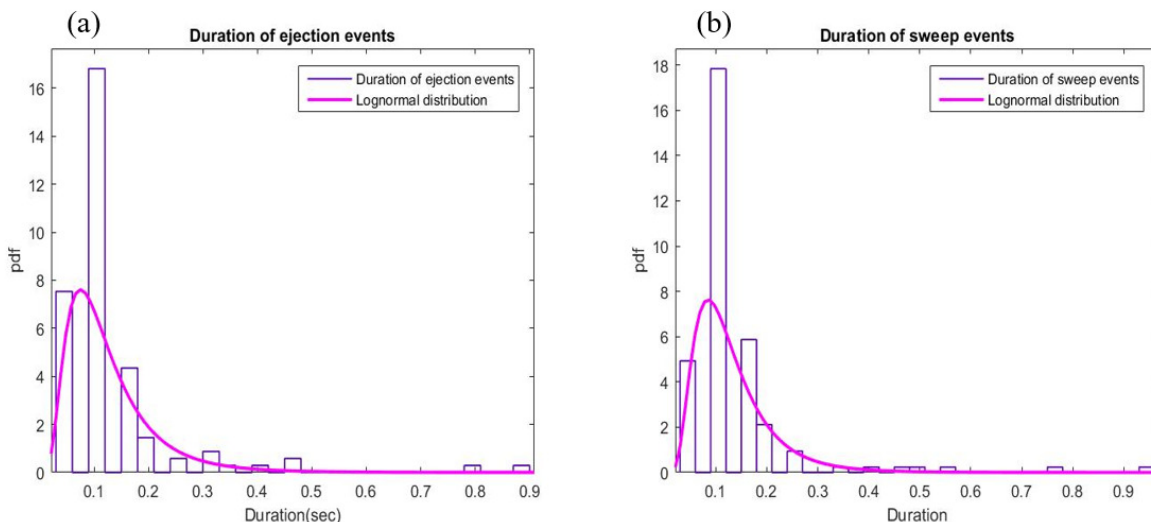
440 detached ejection events exhibit different distribution trends, as displayed in **Figure 8(b)** and (d).
441 As presented in **Figure 8(b)**, while the attached ejection event occurs, its spatial distribution tends
442 to become more significant in both directions, which is consistent with the tall wall-attached
443 structures observed by Yoon et al. (2020). The distributions of sweep and ejection events are
444 similar to the distributions of detached sweep and ejection events, respectively.

445 7.2 Duration of LSMs and the Occurrence Ratio of Sweep Events to Ejection Events

446 Although ejection and sweep event durations can be determined using quadrant analysis or
447 other criteria as each event passes through a single measurement point, the duration of the
448 persistence of such events is difficult to be obtained using a point-wise measurement because an
449 event may continue after a single measurement point passes.

450 Laskari et al. (2018) studied the time evolution of UMZs in the TBL and provided a
451 residence time for LSMs. The concept of residence time differs considerably from the concepts of
452 duration and lifespan. Liu et al. (2016) provided a sketch of duration, maximum shear stress,
453 transport momentum, and period. Residence time is not identical to a period, which is the interval
454 between two events. Herein, the duration of every event is directly tracked using the JHTDB,
455 which yields the result presented in **Figure 9**.

456 Both events exhibit similar residence time distributions. Noguchi and Nezu (2009) also
457 observed that both events exhibit similar duration distributions. In the current analysis, the duration
458 distributions of ejection and sweep events are nearly identical. Consistent with the observation of
459 Noguchi and Nezu (2009), the lifespan of coherent structures is a lognormal distribution.
460



461 **Figure 9.** The probability density function of the duration (lifespan) of (a) ejection and (b)
462 sweep events.
463
464

465 Regarding the occurrence ratio of ejection and sweep events along the normal-wall
466 direction, Sun et al. (2019) observed that both the ratio of the ejection number to the total number
467 of ejection and sweep events and that of the sweep number to the total number of ejection and
468 sweep events declined with the increase of the wall-normal position in clear water condition. The
469 number of ejection events was lower than that of sweep events; that is, the occurrence ratio of
470 sweep events was higher than that of ejection events, which is consistent with the information we

471 extracted from the JHTDB (the occurrence ratio of sweep events was approximately 55-60%). In
 472 UMZs, an ejection event is not guaranteed to occur when a sweep event occurs. Moreover, we also
 473 determined an occurrence ratio of sweep events of 55%–60% under the condition that both ejection
 474 and sweep events have already occurred in each UMZ edge. **Table 2** summarizes the observations
 475 on the sweep and ejection events from the DNS data in this study.

476
 477

Table 2. Characteristics of Q_2 and Q_4 events

Characterization of Q_2 and Q_4 events	Observations	
	Q_2 (Ejection event)	Q_4 (Sweep event)
Location of event occurrences	y^+ between 1100 and 2200 below the UMZ edges	y^+ above 4,400 above the UMZ edges
Attached and detached events	Primarily attached events (appear in the near-wall)	Primarily detached events (appear away from the wall)
Joint PDFs of L_x and L_y	more extensive in vertical variation	longer streamwise length
PDF of event durations	lognormal distribution	lognormal distribution
Occurrence Ratio	40%~45%	55%~60%

478 **8. Conclusions**

479 The existence of UMZs has been demonstrated to be crucial when determining the spatial
 480 distribution of coherent structures of LSMs in wall-bounded turbulence. Most studies have
 481 emphasized that LSMs such as ejection and sweep events in turbulence contribute to the
 482 probabilistic behaviors of turbulence, and subsequently, transport of sediment particles. Therefore,
 483 in the current study, conditional velocity decomposition in which the mean velocity is a function
 484 of wall-normal distance and UMZ edge height was used to capture coherent structures in the flow
 485 field. The structure of the wall-bounded turbulent flow based on the DNS data established by Lee
 486 and Moser (2014) was analyzed in this study.

487 In the current study, several criteria for identifying the turbulent coherent structures are
 488 revisited. A standard procedure that focuses on the spatial-temporal distribution of ejection and
 489 sweep events in wall-bounded flow is established. Fisceletti and Ganapathisubramani (2018)
 490 proposed a criterion for distinguishing two arbitrary structures at two consecutive time steps,
 491 which we used to track the duration of each structure. This criterion was also used to discriminate
 492 and extract structures throughout the flow field in a single timestep. LSMs were then reliably
 493 extracted from wall-bounded turbulent flow and tracked by applying the integrated criteria as
 494 proposed in this study. Sweep and ejection event characterization, such as the probability
 495 distributions of event durations and streamwise length and wall-normal length, as well as the
 496 occurrence ratio, were quantified and then further compared with those reported in other studies.

497 Regarding the spatial properties of LSMs, the effect of the UMZ edges, which constrain
 498 the vertical development of LSMs, was considered. The scale of the wall-normal length (L_y) was
 499 consistent with that of observations of other wall-bounded flow. Yoon et al. (2020) revealed that
 500 most L_y ranges from 0.4δ to 0.6δ . However, some disparity was observed between our analysis
 501 and that of Dennis and Nickels (2011), which might be attributed to the essential difference in their
 502 flow conditions. The probability distributions of the maximum height, wall-normal length and

503 streamwise length of the coherent structures can be determined. Moreover, the joint probability
504 distributions of the wall-normal and streamwise length of the sweep and ejection events
505 respectively can be further established.

506 It is discovered that the distribution of detached sweep events is more similar to the
507 distribution of entire sweep events. This phenomenon confirms the finding that sweep events
508 appear away from the wall and drop to dissipate. Accordingly, sweep events are commonly named
509 detached structures. By contrast, attached and detached ejection events exhibit different
510 distribution trends. While the attached ejection event occurs, its spatial distribution tends to
511 become larger in both directions. However, despite the spatial-resolution of LSMs being
512 insufficient for capturing the real distribution of the streamwise length of structures because of its
513 tendency to merge two structures in the streamwise direction, our observation confirms that
514 VLSMs consist of LSMs. This result further reveals that LSM duration follows a lognormal
515 distribution based on best fit, which is consistent with Noguchi and Nezu's (2009) findings. It is
516 also found that an occurrence ratio of sweep events of 55%–60% under the condition that both
517 ejection and sweep events can be observed occurred in each UMZ edge.

518 The organized vortical structures that contort UMZ interfaces are a manifestation of
519 ejection events and sweep events around the interface, demonstrating that UMZ edges and the
520 spatial distribution of LSMs affect each other. In this study, discrimination of the interfaces of
521 UMZs is viewed as an essential step in estimating the spatial and temporal scales and other
522 properties of LSMs. It is expected that our understanding of probabilistic characteristics of sweep
523 and ejection coherent structures can be enhanced. With the better characterization of the random
524 and intermittent behaviors of turbulent coherent structures, a complete description of sediment
525 particle movement in turbulent flows can then be made available.

526 **Acknowledgments**

528 The authors thank the Ministry of Science and Technology of Taiwan for financially supporting
529 this research under the contract numbers MOST 107-2628-E-002-002-MY3 and 108-2221-E-002-
530 011-MY3. The authors would like to acknowledge the accessibility of the extensive database at
531 Johns Hopkins Turbulence Database (JHTDB).

532 **Data Availability**

534 All the turbulence flow data used in this study are available at the Johns Hopkins Turbulence
535 Database website funded by National Science Foundation <http://turbulence.pha.jhu.edu>.

536
537
538
539
540
541
542
543
544
545
546
547
548

549 **References**

- 550 Adrian, R., Christensen, K., & Liu, Z.-C. (2000). Analysis and interpretation of instantaneous
551 turbulent velocity fields. *Experiments in Fluids*, 29(3), 275-290.
- 552 Adrian, R. J., & Marusic, I. (2012). Coherent structures in flow over hydraulic engineering surfaces.
553 *Journal of Hydraulic Research*, 50(5), 451-464.
- 554 Adrian, R. J., Meinhardt, C. D., & Tomkins, C. D. (2000). Vortex organization in the outer region
555 of the turbulent boundary layer. *Journal of Fluid Mechanics*, 422, 1-54.
- 556 Antonia, R. (1972). Conditionally sampled measurements near the outer edge of a turbulent
557 boundary layer. *Journal of Fluid Mechanics*, 56(1), 1-18.
- 558 Antonia, R., Prabhu, A., & Stephenson, S. (1975). Conditionally sampled measurements in a
559 heated turbulent jet. *Journal of Fluid Mechanics*, 72(3), 455-480.
- 560 Blackwelder, R. F., & Eckelmann, H. (1979). Streamwise vortices associated with the bursting
561 phenomenon. *Journal of Fluid Mechanics*, 94(3), 577-594.
- 562 Cellino, M., & Lemmin, U. (2004). Influence of coherent flow structures on the dynamics of
563 suspended sediment transport in open-channel flow. *Journal of Hydraulic Engineering*, 130(11),
564 1077-1088.
- 565 Chang, W., Constantinescu, G., Tsai, W., & Lien, H. (2011). Coherent structure dynamics and
566 sediment erosion mechanisms around an in-stream rectangular cylinder at low and moderate angles
567 of attack. *Water Resources Research*, 47(12).
- 568 Chen, D., Sun, H., & Zhang, Y. (2013). Fractional dispersion equation for sediment suspension.
569 *Journal of Hydrology*, 491, 13-22.
- 570 Chen, Q., Zhong, Q., Qi, M., & Wang, X. (2015). Comparison of vortex identification criteria for
571 planar velocity fields in wall turbulence. *Physics of Fluids*, 27(8), 085101.
- 572 de Silva, C. M., Hutchins, N., & Marusic, I. (2016). Uniform momentum zones in turbulent
573 boundary layers. *Journal of Fluid Mechanics*, 786, 309.
- 574 de Silva, C. M., Philip, J., Hutchins, N., & Marusic, I. (2017). Interfaces of uniform momentum
575 zones in turbulent boundary layers.
- 576 Dennis, D. J., & Nickels, T. B. (2011). Experimental measurement of large-scale three-dimensional
577 structures in a turbulent boundary layer. Part 2. Long structures. *Journal of Fluid Mechanics*, 673,
578 218.
- 579 Dwivedi, A., Melville, B. W., Shamseldin, A. Y., & Guha, T. K. (2011). Flow structures and
580 hydrodynamic force during sediment entrainment. *Water Resources Research*, 47(1).
- 581 Eisma, J., Westerweel, J., Ooms, G., & Elsinga, G. E. (2015). Interfaces and internal layers in a
582 turbulent boundary layer. *Physics of Fluids*, 27(5), 055103.
- 583 Fabris, G. (1979). Conditional sampling study of the turbulent wake of a cylinder. Part 1. *Journal*
584 *of Fluid Mechanics*, 94(4), 673-709.
- 585 Falco, R. E. (1977). Coherent motions in the outer region of turbulent boundary layers. *The Physics*
586 *of Fluids*, 20(10), S124-S132.
- 587 Ferreira, R., Leal, J., & Cardoso, A. (2002). Turbulent structures and near-bed sediment transport

588 in open-channel flows. *River Flow* 2002, 1, 553-563.

589 Fiscaletti, D., & Ganapathisubramani, B. (2018). Characteristics of sources and sinks of
590 momentum in a turbulent boundary layer. *Physical Review Fluids*, 3(5), 054601.

591 Franca, M. J., Santos, B., Antico, F., & Ferreira, R. (2014). Quadrant analysis of shear events in
592 open channel flows over mobile and immobile hydraulically rough beds. *ERCOFTAC Bulletin*,
593 100(ARTICLE), 29-36.

594 Ganapathisubramani, B., Longmire, E. K., & Marusic, I. (2003). Characteristics of vortex packets
595 in turbulent boundary layers.

596 Grass, A. J. (1971). Structural features of turbulent flow over smooth and rough boundaries.
597 *Journal of Fluid Mechanics*, 50(2), 233-255.

598 Gutmark, E., & Wignanski, I. (1976). The planar turbulent jet. *Journal of Fluid Mechanics*, 73(3),
599 465-495.

600 Hedley, T. B., & Keffer, J. F. (1974). Some turbulent/non-turbulent properties of the outer
601 intermittent region of a boundary layer. *Journal of Fluid Mechanics*, 64(4), 645-678.

602 Hurther, D., & Lemmin, U. (2003). Turbulent particle flux and momentum flux statistics in
603 suspension flow. *Water Resources Research*, 39(5).

604 Hutchins, N., & Marusic, I. (2007). Large-scale influences in near-wall turbulence. *Philosophical
605 Transactions of the Royal Society A: Mathematical, Physical and Engineering Sciences*, 365(1852),
606 647-664.

607 JCR, H., Wray, A., & Moin, P. (1988). Eddies, stream, and convergence zones in turbulent flows.
608 Center for turbulence research report CTR-S88, 193-208.

609 Jeong, J., & Hussain, F. (1995). On the identification of a vortex. *Journal of fluid mechanics*, 285,
610 69-94.

611 Jeong, J., Hussain, F., Schoppa, W., & Kim, J. (1997). Coherent structures near the wall in a
612 turbulent channel flow. *Journal of Fluid Mechanics*, 332(185-214), 188.

613 Juan, C., ALAMO, J. J. E., Jiménez, J., Zandonade, P., & Moser, R. (2006). Self-similar vortex
614 clusters in the turbulent logarithmic region. *J. Fluid Mech*, 561, 329-358.

615 Kaftori, D., Hetsroni, G., & Banerjee, S. (1994). Funnel-shaped vortical structures in wall
616 turbulence. *Physics of Fluids*, 6(9), 3035-3050.

617 Kim, K., & Adrian, R. (1999). Very large-scale motion in the outer layer. *Physics of Fluids*, 11(2),
618 417-422.

619 Kwon, Y., Hutchins, N., & Monty, J. (2016). On the use of the Reynolds decomposition in the
620 intermittent region of turbulent boundary layers. *Journal of Fluid Mechanics*, 794, 5.

621 Laskari, A., de Kat, R., Hearst, R. J., & Ganapathisubramani, B. (2018). Time evolution of uniform
622 moment zones in a turbulent boundary layer.

623 Lee, J., Sung, H. J., & Zaki, T. A. (2017). Signature of large-scale motions on turbulent/non-
624 turbulent interface in boundary layers. *Journal of Fluid Mechanics*, 819, 165.

625 Lee, M., & Moser, R. D. (2014). Direct numerical simulation of turbulent channel flow up to
626 $Re_\tau \approx 5200$. *Journal of Fluid Mechanics*. 774, 395-415.

- 627 LeHew, J., Guala, M., & McKeon, B. (2013). Time-resolved measurements of coherent structures
628 in the turbulent boundary layer. *Experiments in Fluids*, 54(4), 1-16.
- 629 Lelouvetel, J., Bigillon, F., Doppler, D., Vinkovic, I., & Champagne, J. Y. (2009). Experimental
630 investigation of ejections and sweeps involved in particle suspension. *Water Resources Research*,
631 45(2).
- 632 Liu, D., Liu, X., Fu, X., & Wang, G. (2016). Quantification of the bed load effects on turbulent
633 open-channel flows. *Journal of Geophysical Research: Earth Surface*, 121(4), 767-789.
- 634 Lozano-Durán, A., Flores, O., & Jiménez, J. (2012). The three-dimensional structure of momentum
635 transfer in turbulent channels, *Journal of Fluid Mechanics*, 694, 100.
- 636 Lozano-Durán, A., & Jiménez, J. (2014). Time-resolved evolution of coherent structures in
637 turbulent channels: characterization of eddies and cascades. *Journal of fluid mechanics*, 759, 432.
- 638 Lu, S., & Willmarth, W. (1973). Measurements of the structure of the Reynolds stress in a turbulent
639 boundary layer. *Journal of Fluid Mechanics*, 60(3), 481-511.
- 640 MacVicar, B., & Roy, A. (2007). Hydrodynamics of a forced riffle pool in a gravel bed river: 2.
641 Scale and structure of coherent turbulent events. *Water Resources Research*, 43(12).
- 642 Meinhart, C. D., & Adrian, R. J. (1995). On the existence of uniform momentum zones in a
643 turbulent boundary layer. *Physics of Fluids*, 7(4), 694-696.
- 644 Moisy, F., & Jiménez, J. (2004). Geometry and clustering of intense structures in isotropic
645 turbulence. *Journal of fluid mechanics*, 513, 111.
- 646 Muste, M., Yu, K., Fujita, I., & Ettema, R. (2005). Two-phase versus mixed-flow perspective on
647 suspended sediment transport in turbulent channel flows. *Water Resources Research*, 41(10).
- 648 Nagaosa, R. (1999). Direct numerical simulation of vortex structures and turbulent scalar transfer
649 across a free surface in a fully developed turbulence. *Physics of Fluids*, 11(6), 1581-1595.
- 650 Nezu, I., Nakagawa, H., & Jirka, G. H. (1994). Turbulence in open-channel flows. *Journal of*
651 *Hydraulic Engineering*, 120(10), 1235-1237.
- 652 Nino, Y., & García, M. (1996). Heuristic model for particle entrainment into suspension.
653 *Proceedings of the 1996 11th Conference on Engineering Mechanics. Part 1 (of 2)*,
- 654 Noguchi, K., & Nezu, I. (2009). Particle-turbulence interaction and local particle concentration in
655 sediment-laden open-channel flows. *Journal of Hydro-environment Research*, 3(2), 54-68.
- 656 Offen, G., & Kline, S. (1975). A proposed model of the bursting process in turbulent boundary
657 layers. *Journal of Fluid Mechanics*, 70(2), 209-228.
- 658 Okamoto, T., Nezu, I., & Katayama, A. (2010). Simultaneous measurements of concentration and
659 velocity with combined PIV and planar LIF in vegetated open-channel flows. *River Flow 2010*,
660 487-494.
- 661 Robinson, S. K. (1991). Coherent motions in the turbulent boundary layer. *Annual Review of Fluid*
662 *Mechanics*, 23(1), 601-639.
- 663 Salim, S., Pattiaratchi, C., Tinoco, R., Coco, G., Hetzel, Y., Wijeratne, S., & Jayaratne, R. (2017).
664 The influence of turbulent bursting on sediment resuspension under unidirectional currents. *Earth*
665 *Surface Dynamics*, 5(3), 399-415.

- 666 Saxton-Fox, T., & McKeon, B. J. (2017). Coherent structures, uniform momentum zones and the
667 streamwise energy spectrum in wall-bounded turbulent flows. *Journal of Fluid Mechanics*, 826.
- 668 Séchet, P., & le Guennec, B. (1999). The role of near wall turbulent structures on sediment
669 transport. *Water Research*, 33(17), 3646-3656.
- 670 She, Z.-S., Jackson, E., & Orszag, S. A. (1990). Intermittent vortex structures in homogeneous
671 isotropic turbulence. *Nature*, 344(6263), 226-228.
- 672 Smits, A. J., McKeon, B. J., & Marusic, I. (2011). High-Reynolds number wall turbulence. *Annual
673 Review of Fluid Mechanics*, 43, 353-375.
- 674 Srinath, S. (2017). Modeling and prediction of near wall turbulent flows Ecole Centrale de Lille].
- 675 Sun, J., Gao, T., Fan, Y., Chen, W., & Xuan, R. (2019). The modulation of particles on coherent
676 structure of turbulent boundary layer in dilute liquid-solid two-phase flow with PIV. *Powder
677 Technology*, 344, 883-896.
- 678 Tomkins, C. D., & Adrian, R. J. (2002). Spanwise structure and scale growth in turbulent boundary
679 layers (0073-5264).
- 680 Truong, S., & Uijttewaal, W. (2019). Transverse momentum exchange induced by large coherent
681 structures in a vegetated compound channel. *Water Resources Research*, 55(1), 589-612.
- 682 Tsai, C. W., & Huang, S. H. (2019). Modeling suspended sediment transport under influence of
683 turbulence ejection and sweep events. *Water Resources Research*, 55(7), 5379-5393.
- 684 Tsai, C. W., Huang, S. H., & Hung, S. Y. (2021). Incorporating the Memory Effect of Turbulence
685 Structures into Suspended Sediment Transport Modeling. *Water Resources Research*, 57(3),
686 e2020WR028475.
- 687 Wallace, J. M., Eckelmann, H., & Brodkey, R. S. (1972). The wall region in turbulent shear flow.
688 *Journal of Fluid Mechanics*, 54(1), 39-48.
- 689 Wang, F., Huai, W., Guo, Y., & Liu, M. (2021). Turbulence Structure and Momentum Exchange in
690 Compound Channel Flows with Shore Ice Covered on the Floodplains. *Water Resources Research*,
691 57(4), e2020WR028621.
- 692 Yoon, M., Hwang, J., Yang, J., & Sung, H. J. (2020). Wall-attached structures of streamwise
693 velocity fluctuations in an adverse-pressure-gradient turbulent boundary layer. *Journal of Fluid
694 Mechanics*, 885.
- 695 Zhong, Q., Chen, Q., Wang, H., Li, D., & Wang, X. (2016). Statistical analysis of turbulent super-
696 streamwise vortices based on observations of streaky structures near the free surface in the smooth
697 open channel flow. *Water Resources Research*, 52(5), 3563-3578.
- 698 Zhou, J., Adrian, R. J., Balachandar, S., & Kendall, T. (1999). Mechanisms for generating coherent
699 packets of hairpin vortices in channel flow. *Journal of Fluid mechanics*, 387, 353-396.